Journal of Micromechanics and Microengineering

A reconfigurable and portable acoustofluidic system based on flexible printed circuit board for the manipulation of microspheres

OPEN ACCESS
IOP Publishing
Journal of Micromechanics and Microengineering
J. Micromech. Microeng. **31** (2021) 074003 (9pp)
https://doi.org/10.1088/1361-6439/ac0515

A reconfigurable and portable acoustofluidic system based on flexible printed circuit board for the manipulation of microspheres

Roman Mikhaylov[1], Mercedes Stringer Martin[1], Povilas Dumcius[1], Hanlin Wang[1], Fangda Wu[1], Xiaoyan Zhang[2], Victory Akhimien[1], Chao Sun[3], Aled Clayton[4], Yongqing Fu[5], Lin Ye[6], Zhiqiang Dong[7], Zhenlin Wu[8] and Xin Yang[1,*]

[1] Department of Electrical and Electronic Engineering, School of Engineering, Cardiff University, Cardiff CF24 3AA, United Kingdom
[2] International Joint Laboratory of Biomedicine and Engineering, Huazhong Agricultural University and Cardiff University, Wuhan, Hubei 430070, People's Republic of China
[3] School of Life Sciences, Northwestern Polytechnical University, Xi'an 710072, People's Republic of China
[4] Tissue Micro-Environment Group, Division of Cancer and Genetics, School of Medicine, Cardiff University, Cardiff CF14 4XN, United Kingdom
[5] Faculty of Engineering and Environment, Northumbria University, Newcastle Upon Tyne NE1 8ST, United Kingdom
[6] Cardiff China Medical Research Collaborative, Division of Cancer and Genetics, School of Medicine, Cardiff University, Cardiff CF14 4XN, United Kingdom
[7] College of Biomedicine and Health, College of Life Science and Technology, Huazhong Agricultural University, Wuhan, Hubei 430070, People's Republic of China
[8] School of Optoelectronic Engineering and Instrumentation Science, Dalian University of Technology, Dalian 116023, People's Republic of China

E-mail: YangX26@cardiff.ac.uk

Received 1 March 2021, revised 7 May 2021
Accepted for publication 25 May 2021
Published 9 June 2021

Abstract

Acoustofluidic devices based on surface acoustic waves (SAWs) have been widely applied in biomedical research for the manipulation and separation of cells. In this work, we develop an accessible manufacturing process to fabricate an acoustofluidic device consisting of a SAW interdigital transducer (IDT) and a polydimethylsiloxane microchannel. The IDT is manufactured using a flexible printed circuit board pre-patterned with interdigital electrodes that is mechanically coupled with a piezoelectric substrate. A new microchannel moulding technique is realised by 3D printing on glass slides and is demonstrated by constructing the microchannel for the acoustofluidic device. The flexible clamping mechanism, used to construct the device, allows the reconfigurable binding between the IDT and the microchannel. This unique construction makes the acoustofluidic device capable of adjusting the angle between the microchannel and the SAW propagation, without refabrication, via either rotating the IDT or the microchannel. The angle adjustment is demonstrated by setting the polystyrene microsphere aggregation angle to −5°, 0°, 6°, and 15°. Acoustic energy density measurements demonstrate

* Author to whom any correspondence should be addressed.

the velocity of microsphere aggregation in the device can be accurately controlled by the input power. The manufacturing process has the advantages of reconfigurability and rapid-prototyping to facilitate preparing acoustofluidic devices for wider applications.

Keywords: acoustofluidics, surface acoustic wave, SAW, FPCB IDEs

(Some figures may appear in colour only in the online journal)

1. Introduction

Acoustofluidic devices have attracted great interest in label-free manipulations of micro- [1] and nano-particles [2] owning to their considerable biocompatibility and precision. They have been demonstrated in biomedical applications for separation (exosomes [3–5], tumour [6], and inflammatory [7] cells), manipulation (cell interaction [8], single cells [9], and *Caenorhabditis* elegans [10]), and stimulation of cells [11].

Surface acoustic wave (SAW) devices are almost independent from the microchannel material in terms of acoustic properties compared to bulk acoustic wave devices [12]. This feature makes them easy to fabricate for high-frequency applications (MHz–GHz) [3, 13] and integrate with other systems, such as microfluidics. SAW devices are conventionally fabricated by patterning interdigital transducers (IDTs) on a piezoelectric substrate [14], which convert radio frequency (RF) signals into SAWs propagating on the surface of the substrate. When the SAW meets a liquid medium, it diffracts into the medium and generates a time-averaged pressure distribution that can be utilised to precisely manipulate micro-objects [15]. Standing SAW (SSAW) devices, constructed by a pair of opposite IDTs working on the same frequency, are primarily used in acoustofluidic applications [16]. A great diversity of manipulation and actuation can be achieved by setting up the IDT structure to create, for example, tilted-angle SSAW devices [17, 18] and 2D- and 3D-patterning tweezers [8, 19–21]. However, IDTs manufactured through conventional techniques, such as photolithography, are permanently patterned on the piezoelectric substrate. Polydimethylsiloxane (PDMS) microchannels, used to accommodate biological samples in acoustofluidic systems, also use the photolithography process involving cleanroom facilities. Thus, acoustofluidic devices capable of manufacturing and reconfiguring in general laboratories, using off-the-shelf components, are highly desired.

A new fabrication technique, developed by our group, has successfully fabricated the IDTs without the use of a cleanroom for the manipulation of microparticles and cancer cells [22]. The IDTs were manufactured by mechanically clamping a rigid printed circuit board (PCB) pre-patterned with interdigital electrodes (IDEs) onto a piezoelectric substrate. This technique has been benchmarked against a device made by conventional photolithography in terms of frequency response, droplet transportation, and cell manipulation. The PCB-based IDT has the advantage of replacing piezoelectric substrates by simply disassembling the mechanically clamped structure, with no need to remanufacture the IDT. Another IDT made by flexible PCB (FPCB) pre-patterned with IDEs demonstrated similar performance with advantages of dynamic flexing, less weight, and better heat dissipation [23].

A development process with low requirement on facilities and operation of the device using a portable control unit can better support broadening the use of the acoustofluidic devices. Herein, we present a novel development technique for both the IDTs and the microchannel, we call it versatile acoustofluidic device (VAD). We also demonstrate the rapid-prototyping and reconfigurability of VAD for precise manipulation of micro-objects.

2. Methods and materials

2.1. FPCBs

The FPCB pre-patterned with IDEs, used in the VAD, was externally manufactured (circuitfly.com) using a standard PCB manufacturing process. The IDEs were made of metal bilayers (Au/Ni, 30 nm/2 μm) patterned on a 70 μm thick polyester laminate. The IDEs consist of 40 pairs of 10 mm long finger electrodes and have a centre-to-centre finger pitch of 200 μm as shown in figure 1(A). The ratio between the finger spacing and finger width is 1:1. A 128° Y-cut 3 inch lithium niobate ($LiNbO_3$) was used as the piezoelectric substrate. The VAD had a Rayleigh mode frequency of ∼19.9 MHz and a 200 μm wavelength. Two coaxial cables were soldered to the buspads of each FPCB IDEs. Matching networks (MNs) based on an LC circuit are used (figure 1(B)), which are essential in reducing the impedance mismatching between the VAD and the driving power amplifiers [22, 23].

2.2. Clamping mechanism

The VAD required a mechanical jig to hold the main components together, including the FPCB IDEs and $LiNbO_3$ substrate. As shown in figure 1(C), the VAD uses a simple clamping mechanism and consists of the following stacking order from the bottom to the top: heatsink (supports the entire device and dissipates heat), temperature sensors (measure the IDT temperature), $LiNbO_3$ (produces SAWs), FPCB IDEs (convert RF to SAWs), silicon pads (evenly distribute the clamping force), localised pressers (apply the clamping force), FSRs (measure the clamping force), FSR roofs (hold and press the FSRs), M5 screws (generate the clamping force) and main holders (hold the whole structure onto the heatsink). Another structure, which consists of an acrylic presser and a microchannel presser, is developed to hold the microchannel between the two IDTs. The FSR roofs, localised pressers, microchannel

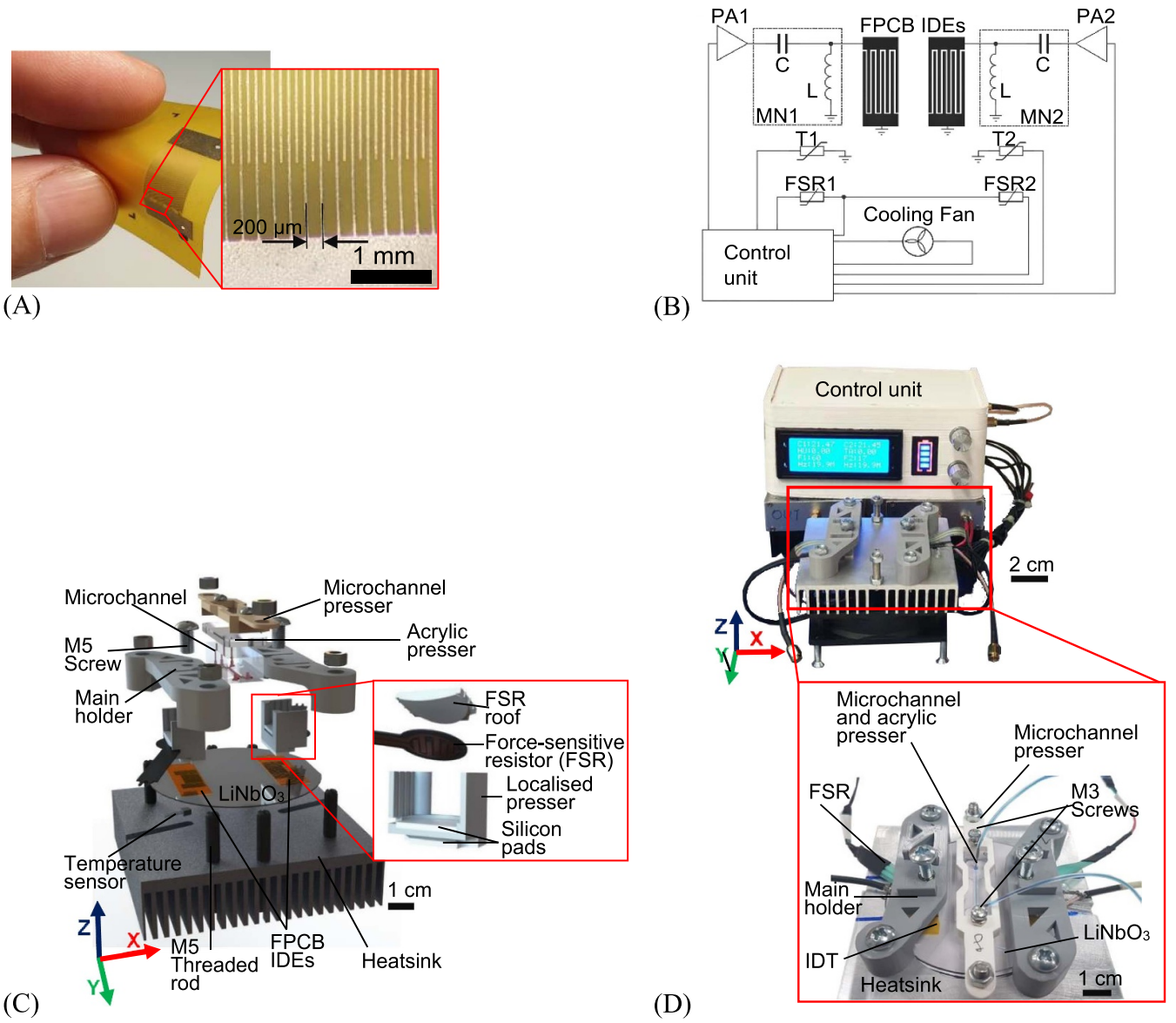

Figure 1. (A) Real-life flexible printed circuit board (FPCB) pre-patterned with IDEs with a zoom inset of the IDEs. (B) Schematic diagram of the VAD and a portable control unit, that can drive a cooling fan and provide RF signals to drive the two IDTs. The RF signals are amplified by two 6 W power amplifiers (PA1 and PA2). Each IDT is connected to a matching network (MN1 and MN2) for impedance matching. The values of the capacitor (C) and inductor (L) are 68 pF and 470 nH, respectively. The sensing components include two temperature sensors (T1 and T2) and force-sensitive resistors (FSR1 and FSR2). (C) 3D exploded view of the VAD with an inset presenting the assembly and components at the localised pressers. (D) The portable control unit and the VAD with an inset demonstrating the real-life model of the assembled VAD on the heatsink.

pressers, and main holders were all 3D printed using a 0.4 mm nozzle and polylactic acid (PLA) filaments.

2.3. The VAD assembly

The FPCB IDEs, microchannel and $LiNbO_3$ substrate were thoroughly cleaned using isopropyl alcohol and de-ionised (DI) water, dried using a compressed air duster and checked under the microscope to ensure that no fibres or dust particles were present on the parts before the final assembly. All the individual components, shown in figure 1(C), are placed on the $LiNbO_3$ which is mounted on the heatsink. A clamping force is created by fastening the two M5 screws on top of the localised pressers. A vector network analyser (VNA) is used to monitor the reflection coefficient (S_{11}) and to confirm when the contact resistance is overcome and an optimal clamping force is achieved [22, 23]. Figure 1(D) shows the final assembled VAD with a portable control unit and an inset to demonstrate the full assembly including the microchannel on the heatsink.

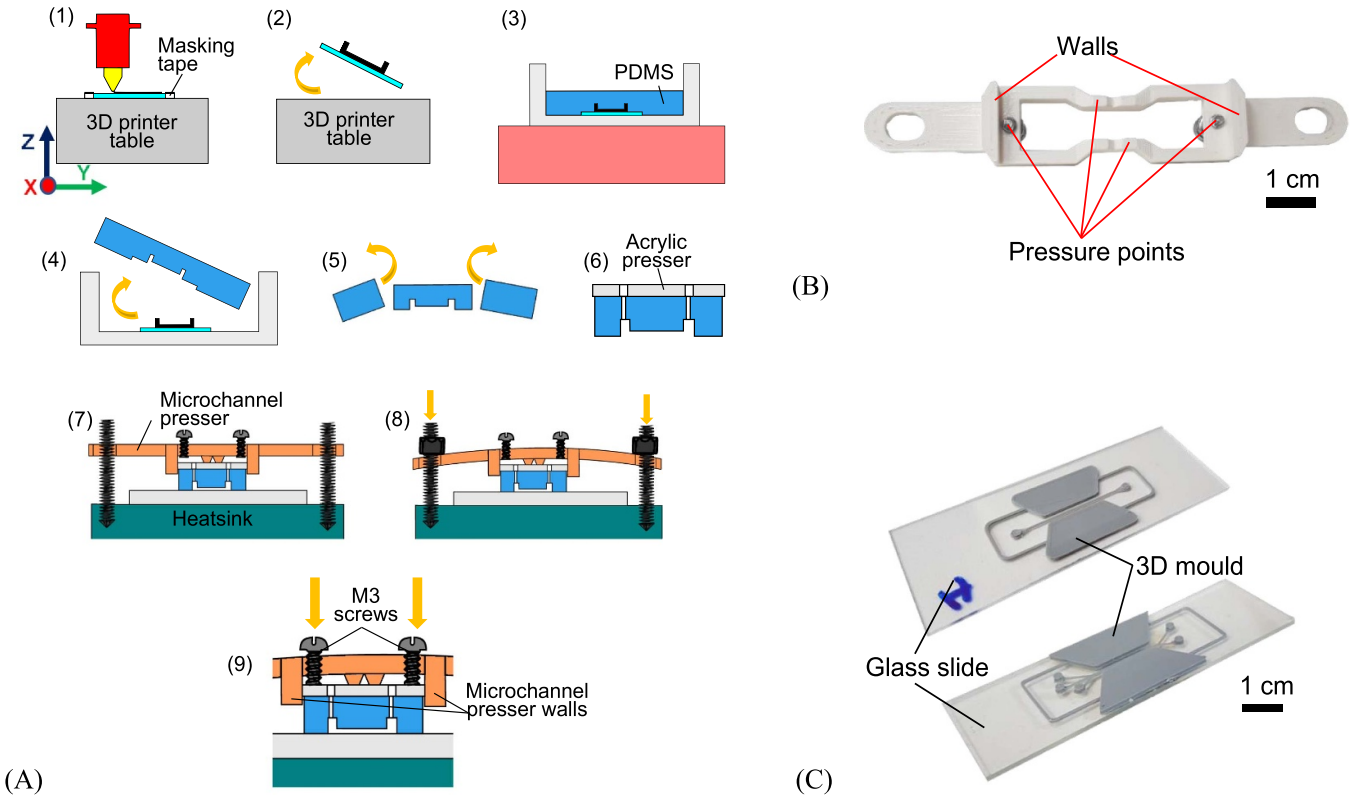

Figure 2. (A) The development steps of the microchannel using the glass-bottom 3D printed mould. (B) The microchannel presser with its the pressure points and walls highlighted. (C) Real-life models of the glass-bottom 3D printed mould.

2.4. Microchannels

The use of a glass-bottom 3D printed mould to prepare the microchannels stands as a novelty for microchannel manufacturing, with the development flow illustrated in figure 2(A). (a) A glass slide (76 mm (W) × 26 mm (L)) is placed on the 3D printer table and held in place using masking tape. A compensatory offset is applied by using a 'Z offset setting' plugin in the 3D printer software. Glass slides with various thicknesses can be used as the glass-bottom of the mould by adjusting the offset setting. The 3D printed mould, designed in Solidworks, is directly printed on the glass slide, (b) removed from the 3D printer table after completion and left to cool. (c) The glass-bottom 3D printed mould is then placed in a plastic petri dish and filled with PDMS (Sylgard 184, Farnell UK), which is prepared according to the manufacturer's protocol. The dish is placed onto a hot plate (SD160, Colepalmer) at a temperature of 45 °C to cure for 24 h, which is below the 60 °C melting temperature of the PLA. (d) The set PDMS is removed from the mould, (e) the outer perimeter of the channel is cut and (f) a premade acrylic presser, with the dimensions of 47 mm (L) × 15 mm (W) × 3 mm (H), is placed on top of the microchannel. (g) The microchannel is then bolted onto the pre-assembled VAD using a microchannel presser (figure 2(B)). (h) The M5 nuts on the far edges of the microchannel presser are fastened until resistance is felt and (i) finally the M3 screws are screwed in to ensure even distribution of the pressing force.

The walls of the microchannel presser (figures 2(A), step 9 and (B)) are created to resist excessive force and prevent it from overbending. These help to keep the force evenly distributed across the microchannel and not to over compress it. To further prevent deformation, the ratio between the PDMS and the microchannel height was 55:1.

Two examples of the glass-bottom 3D printed moulds are shown in figure 2(C), which are single inlet/outlet and three-inlet-two-outlet structures, respectively. Five 3D printed moulds were printed on the same glass slide and measured using a microscope to determine the repeatability of the print.

2.5. Control unit

To increase the portability of the acoustofluidic system and facilitate on-demand use of the VAD, a portable control unit that includes a waveform generator, a power amplifier, a microcontroller, sensors, a display, and a power supply is developed (figure 3).

2.6. Coating and sample preparation

The microchannels were all coated with 1% (w/w) bovine serum albumin solution for 10 min and then flushed with DI water. For the microsphere test, 10 μm polystyrene microspheres (Sigma Aldrich) were used and suspended in a 23%

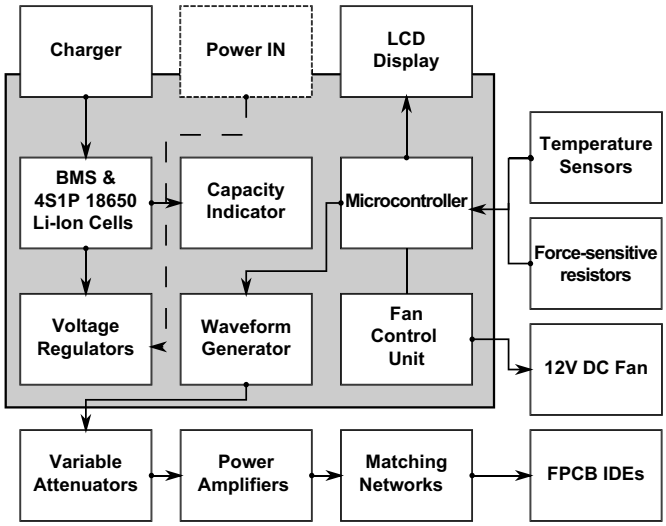

Figure 3. The respective block schematic demonstrating all the internal and external components of the control unit.

(v/v) glycerol and phosphate-buffered saline solution. The microsphere suspension was injected into the microchannels through a syringe.

2.7. IDT alignment setup and analysis

The formation of SSAW relies on the alignment of the two IDTs, which can be reflected by the device's insertion loss (S_{21}). The smaller the insertion loss, the better the SAW transmission from one IDT to another. Thus, one can effectively use the VNA to estimate the IDT alignment. This is demonstrated by connecting two IDTs to the VNA as a two-port network, as shown in figure 4. The test keeps one of the IDTs unmoved, as the receiving IDT, while rotating the other IDT, as the transmitting IDT. The S_{11} of the transmitting IDT is measured during this procedure to monitor how it changes with the rotation. Top view images of the transmitting IDT at different orientations were captured by an overhead camera, which were then analysed using a customised MATLAB code that extracted the angle between the two IDTs. Five reference angles, 17°, 11°, 6°, 2°, and 0°, were determined for the S_{21} readings, which were selected by finding the most observable change in the S_{21}.

2.8. Acoustic energy density analysis

To characterise the acoustic energy density inside the VAD, a MATLAB code adapted from Barnkob *et al* [24] was applied to analyse the trajectory of microspheres. In short, image frames extracted from microscope-captured movies, during the microsphere aggregation process, were analysed for pixel intensity near the pressure node (PN) line. The last frame of each movie was used as the maximum intensity frame. The normalised intensity and the relative intensity of each middle-process frames were then calculated and fit into an expression using a fitting parameter.

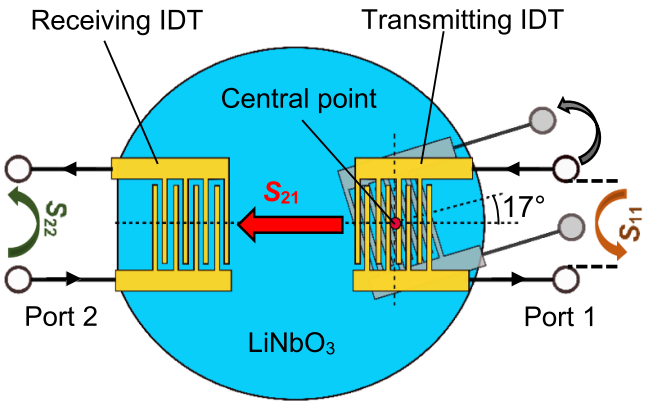

Figure 4. IDT rotation test for investigating the use of the VNA to register the alignment of the IDTs. The transmitting IDT being rotated around its central point, while the receiving IDT is held fixed.

3. Results and discussion

3.1. IDT alignment

Compared to cleanroom made SSAW devices, the VAD depended on the manual alignment of the two IDTs to produce an accurate SSAW and form an even distribution of PN and pressure anti-node lines. The S_{21} peak can be used to establish the angle of the IDTs, where the 0° angle achieves the maximum S_{21} peak as shown in figure 5(A). The S_{11} of the transmitting IDT shows a dip of −28 dB when the two IDTs are in parallel (figure 5(B)), which is within an acceptable working range of conventional SAW devices [25].

3.2. Microchannel characterisation

Figure 6(A) shows the average height and width of the 3D printed moulds, i.e. 102.8 ± 11.4 μm (mean ± SD) and 451.4 ± 42.6 μm (mean ± SD), respectively. Of which a 500 μm wide 3D printed mould is used to produce the microchannel for the following tests (figure 6(B)). The bonding strength of the assembled microchannel met the high throughput requirement by flushing a sample at a flow rate of up to 6 ml min^{-1} [26].

3.3. Acoustic energy density within the VAD

The acoustic energy density of the VAD at 0° is registered at 15, 20 and 27 dBm input power, as the results shown in figures 7(A)–(C), respectively. The time lapse required for 99% of microspheres to aggregate on the PN line is ∼1.9, ∼0.6, and ∼0.3 s for the three input powers. The average acoustic energy density of the powers is shown in figure 7(D), which indicates that the acoustic radiation force exerted on the microspheres can be fully controlled by tuning the input power.

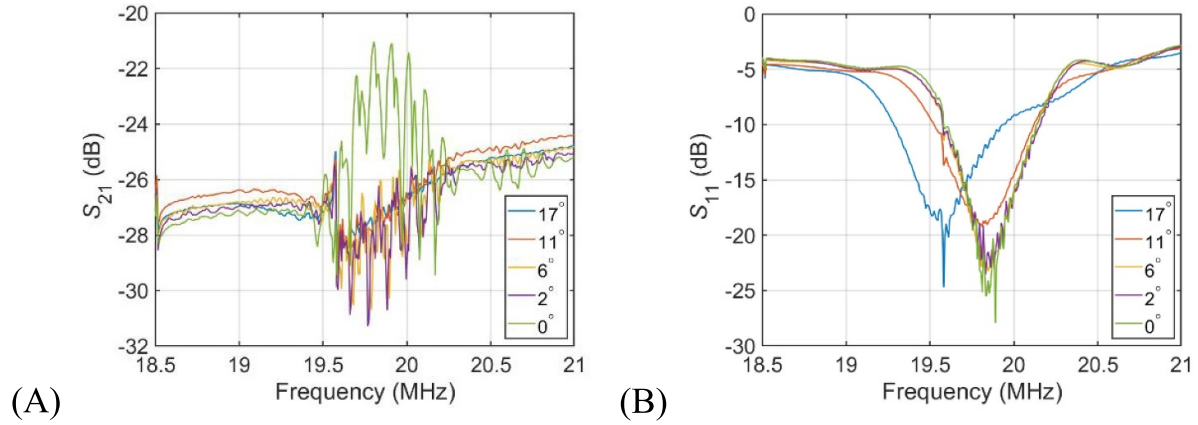

Figure 5. *S*-parameters of the VAD during the rotation of one IDT. (A) Average insertion loss (S_{21}) for each different angle during the rotation. (B) Average reflection coefficient (S_{11}) for each different angle during the rotation.

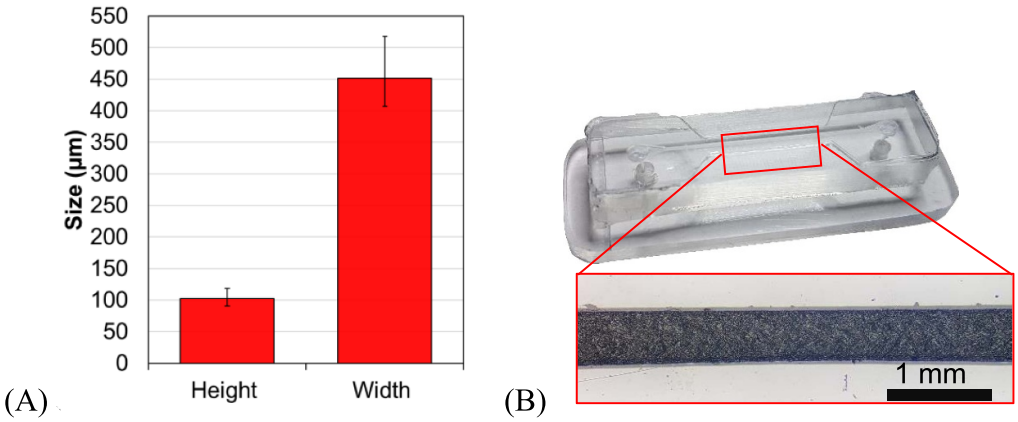

Figure 6. (A) The 3D printed mould's average height and width of 102.8 ± 11.4 μm (mean ± SD) and 451.4 ± 42.6 μm (mean ± SD), respectively. (B) Real-life model of a 500 μm wide microchannel sitting on top of the acrylic presser.

3.4. Rotating the IDTs to adjust the tilted-angle

The VAD can offer reconfigurable tilted-angles (angle between the PN lines and the microchannel) without the need of fabricating new devices. The optimal tilted-angle degree in cell separation depends on the sample flow rate, where a high tilted-angle is optimal for the flow rate of 25 μl min^{-1} and a low tilted-angle for 50–125 μl min^{-1} [6]. The ability of VAD to vary the tilted-angle can potentially save considerable manufacturing effort and cost in reconfiguring devices for versatile and flexible applications. By simply rotating one of the IDTs, we manage to configure the PN lines orientation into two tilted-angles, 0° and 6°, illustrated by the microsphere aggregation shown in figures 8(A) and (B), respectively. The results demonstrate the ability of the VAD in rapid reconfiguration of the tilted-angle to tackle different applications.

3.5. Visually guided assembly of the VAD

The VAD is tested for whether visually aligning the two opposite IDTs by eye can achieve similar performance as the VNA guided assembly. The VAD is assembled visually using the FSRs readings as reference. The alignment quality, represented by the S_{21}, is shown in figure 9(A). Comparing with the VNA guided alignments (blue curve), the visually guided alignments (orange curve) present a smaller S_{21}. Figure 9(B) shows the acoustic energy density is slightly higher in the visually guided assembly. This could be because the distance between the opposing IDTs may have been reduced during the visual experiments [6]. Since the IDTs are pushed further forward to expose their front edge and allow them to be easily visually aligned.

In addition, we collected the microsphere aggregation image for the visually guided assembly, as shown in figure 9(C), which achieves a similar pattern as that in the VNA guided assembly (figure 8(A)). Overall, this confirms that the assembling process of the VAD can be achieved by the visual alignment of the two IDTs without the use of the VNA.

3.6. Rotating the microchannel

The unique construction of the VAD allows an alternative way to alter the tilted-angle by rotating the microchannel clamped to the VAD. New microchannel pressers are printed with two degrees including 15° and −5° to accommodate a wider microchannel as shown in figure 10(A). These pressers are utilised to clamp the microchannel and to create

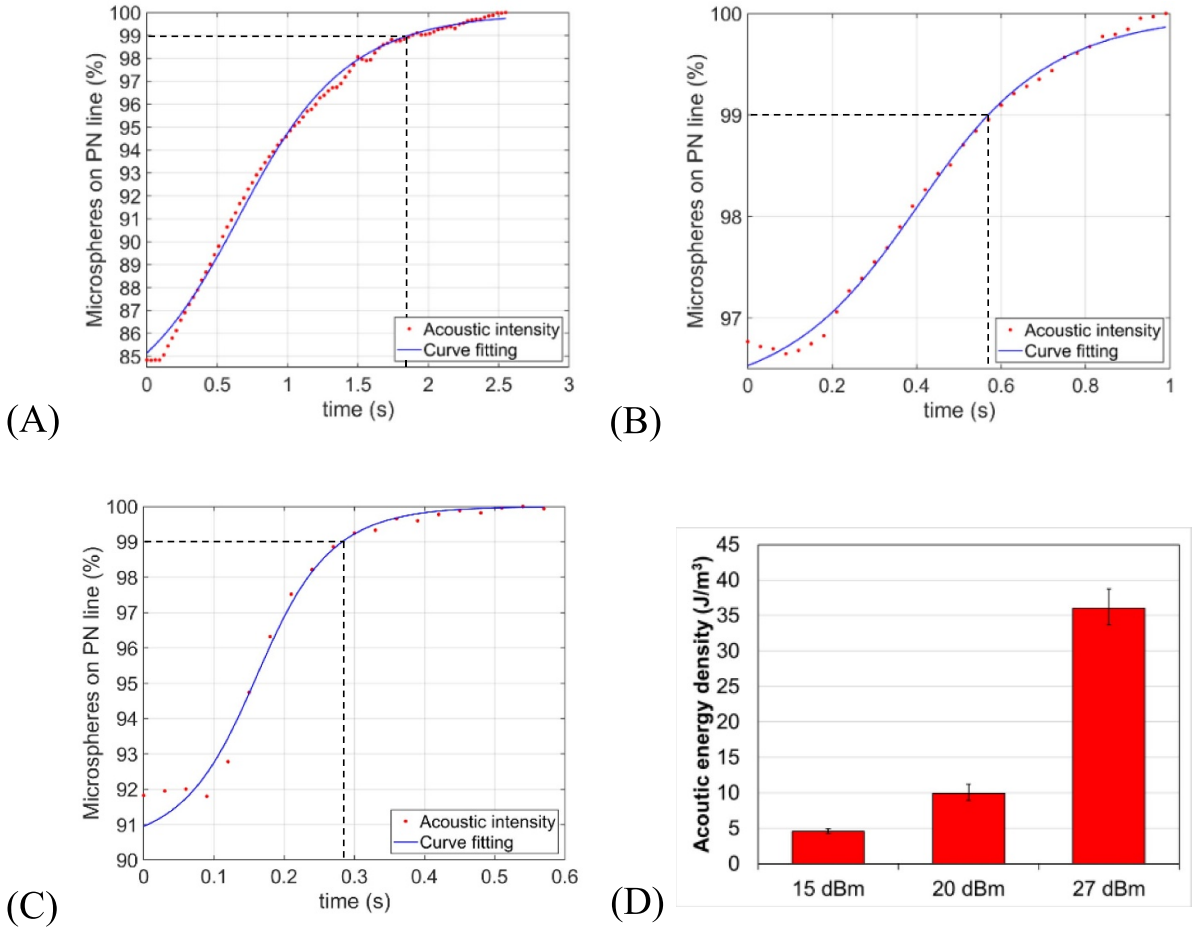

Figure 7. Acoustic energy density of the VAD with parallel IDTs. (A)–(C) Under the input power of 15 dBm, 20 dBm, and 27 dBm, the time for 99% of microspheres to reach the PN line is ∼1.9, ∼0.6, and ∼0.3 s, respectively. (D) The average acoustic energy densities for the three input powers are 4.6, 9.9, and 36 J m^{-3}, respectively ($n = 3$).

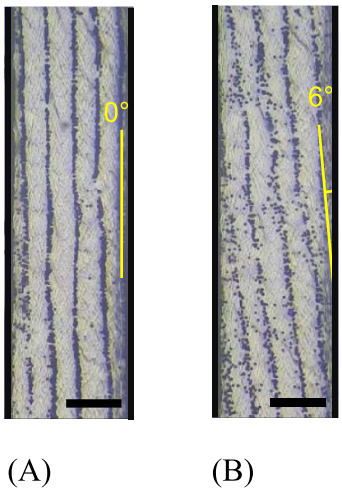

Figure 8. Microscope images showing the reconfigurability of the VAD in setting the PN lines to (A) 0° and (B) 6°. The microspheres are aggregated on the PN lines exhibiting the angle against the wall of the microchannel. (200 μm scale bar).

the respective inclinations for aggregating the microspheres, as shown in figure 10(B).

It is noted that the reconfiguration of the tilted-angles can be achieved by either rotating the microchannel or the IDTs. It may be preferable to rotate the microchannel as it does not require to rotate the IDT, which may potentially affect the frequency response of the VAD.

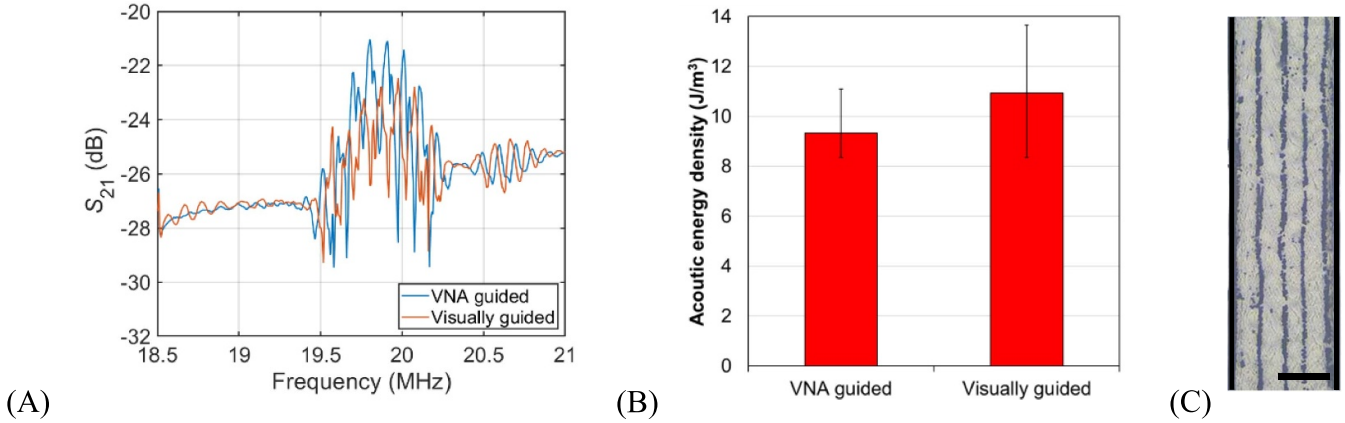

Figure 9. (A) The S_{21} of the VAD assembled using the VNA and the visually guided assembly of the two IDTs. ($n = 5$) (B) Acoustic energy density of the VAD constructed by the two assembly methods, VNA and visually, with an acoustic energy of 9.3 ± 1.2 J m^{-3} (mean $\pm$ SD) and 10.9 ± 2.7 J m^{-3} (mean $\pm$ SD), respectively. ($n = 3$) (C) Microsphere aggregation on the PN lines of the VAD constructed by visually guided assembly (200 μm scale bar).

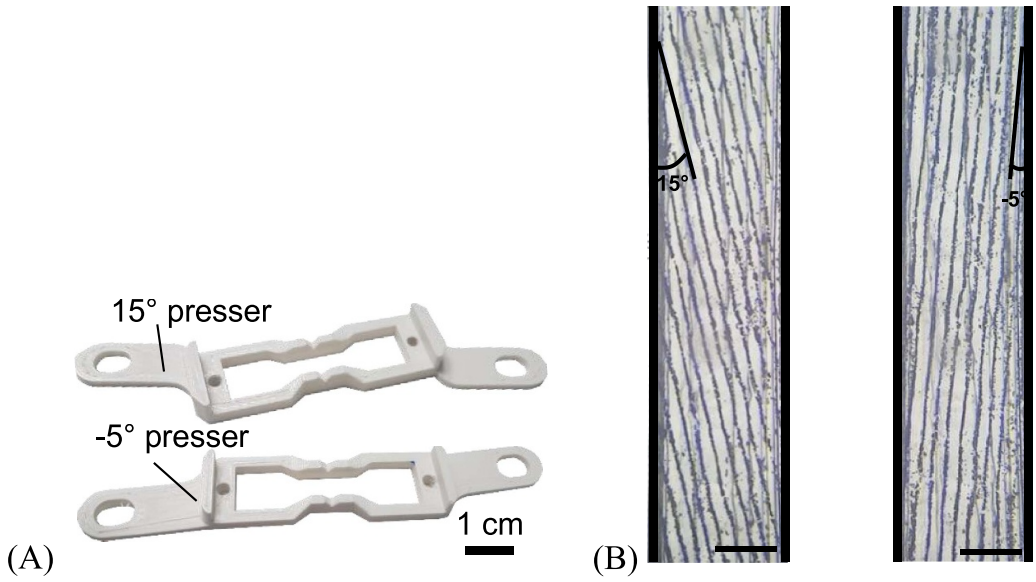

Figure 10. Rotating the microchannel to a set tilted-angle. (A) 3D printed 15° and −5° microchannel pressers. (B) Aggregated microspheres on the PN lines of 15° (left) and −5° (right) angles, in regard to the microchannel wall (450 μm scale bar).

4. Conclusion

This paper introduced a novel technology to manufacture the SAW-based acoustofluidic system, including both the SAW IDT and the PDMS microchannel, without the need of a cleanroom facility. It was demonstrated that a pair of FPCB IDEs were mechanically coupled to the piezoelectric substrate to produce SSAWs, under the guide of either eyes or the VNA. The VAD offers great flexibility in resetting the tilted-angle between the IDTs and the microchannel, resulting in rotatable PN lines inside the acoustofluidic device. The VAD can accomplish a rapid acoustofluidic prototyping process as an alternative to the conventional cleanroom process.

Data availability statement

All data that support the findings of this study are included within the article (and any supplementary files).

Acknowledgments

The authors would gratefully acknowledge the financial support from EPSRC (EP/P002803/1, EP/P018998/1), EPSRC IAA, Welcome Trust, Global Challenges Research Fund (GCRF), the Royal Society (IEC/NSFC/170142, IE161019), and the Natural Science Foundation of China (NSFC) (Grant No. 51811530310).

ORCID iDs

Povilas Dumcius https://orcid.org/0000-0003-2116-1148
Xin Yang https://orcid.org/0000-0002-8429-7598

References

[1] Tian Z *et al* 2019 Wave number–spiral acoustic tweezers for dynamic and reconfigurable manipulation of particles and cells *Sci. Adv.* **5** eaau6062
[2] Wu M, Mao Z, Chen K, Bachman H, Chen Y, Rufo J, Ren L, Li P, Wang L and Huang T J 2017 Acoustic separation of nanoparticles in continuous flow *Adv. Funct. Mater.* **27** 1606039
[3] Wu M *et al* 2017 Isolation of exosomes from whole blood by integrating acoustics and microfluidics *Proc. Natl Acad. Sci. USA* **114** 10584–9
[4] Wu M, Chen C, Wang Z, Bachman H, Ouyang Y, Huang P-H, Sadovsky Y and Huang T J 2019 Separating extracellular vesicles and lipoproteins via acoustofluidics *Lab Chip* **19** 1174–82
[5] Gu Y *et al* 2021 Acoustofluidic centrifuge for nanoparticle enrichment and separation *Sci. Adv.* **7** eabc0467
[6] Li P *et al* 2015 Acoustic separation of circulating tumor cells *Proc. Natl Acad. Sci.* **112** 4970–5
[7] Li S, Ren L, Huang P-H, Yao X, Cuento R A, McCoy J P, Cameron C E, Levine S J and Huang T J 2016 Acoustofluidic transfer of inflammatory cells from human sputum samples *Anal. Chem.* **88** 5655–61
[8] Guo F, Li P, French J B, Mao Z, Zhao H, Li S, Nama N, Fick J R, Benkovic S J and Huang T J 2015 Controlling cell–cell interactions using surface acoustic waves *Proc. Natl Acad. Sci.* **112** 43–8
[9] Ahmed D, Ozcelik A, Bojanala N, Nama N, Upadhyay A, Chen Y, Hanna-Rose W and Huang T J 2016 Rotational manipulation of single cells and organisms using acoustic waves *Nat. Commun.* **7** 11085
[10] Zhang J *et al* 2019 Surface acoustic waves enable rotational manipulation of *Caenorhabditis elegans Lab Chip* **19** 984–92
[11] Ambattu L A, Ramesan S, Dekiwadia C, Hanssen E, Li H and Yeo L Y 2020 High frequency acoustic cell stimulation promotes exosome generation regulated by a calcium-dependent mechanism *Commun. Biol.* **3** 553
[12] Xu K, Clark C P, Poe B L, Lounsbury J A, Nilsson J, Laurell T and Landers J P 2019 Isolation of a low number of sperm cells from female DNA in a glass–PDMS–glass microchip via bead-assisted acoustic differential extraction *Anal. Chem.* **91** 2186–91
[13] Shilton R J, Travagliati M, Beltram F and Cecchini M 2014 Nanoliter-droplet acoustic streaming via ultra high frequency surface acoustic waves *Adv. Mater.* **26** 4941–6
[14] Ai Y, Sanders C K and Marrone B L 2013 Separation of *Escherichia coli* bacteria from peripheral blood mononuclear cells using standing surface acoustic waves *Anal. Chem.* **85** 9126–34
[15] Nama N, Barnkob R, Mao Z, Kähler C J, Costanzo F and Huang T J 2015 Numerical study of acoustophoretic motion of particles in a PDMS microchannel driven by surface acoustic waves *Lab Chip* **15** 2700–9
[16] Ozcelik A, Rufo J, Guo F, Gu Y, Li P, Lata J and Huang T J 2018 Acoustic tweezers for the life sciences *Nat. Methods* **15** 1021
[17] Liu G, He F, Li Y, Zhao H, Li X, Tang H, Li Z, Yang Z and Zhang Y 2019 Effects of two surface acoustic wave sorting chips on particles multi-level sorting *Biomed. Microdevices* **21** 59
[18] Hyun K-A, Gwak H, Lee J, Kwak B and Jung H-I 2018 Salivary exosome and cell-free DNA for cancer detection *Micromachines* **9** 340
[19] Wang Y, Han C and Mei D 2019 Standing surface acoustic wave-assisted fabrication of region-selective microstructures via user-defined waveguides *Langmuir* **35** 11225–31
[20] Guo F *et al* 2016 Three-dimensional manipulation of single cells using surface acoustic waves *Proc. Natl Acad. Sci.* **113** 1522–7
[21] Nguyen T D, Tran V T, Fu Y Q and Du H 2018 Patterning and manipulating microparticles into a three-dimensional matrix using standing surface acoustic waves *Appl. Phys. Lett.* **112** 213507
[22] Mikhaylov R *et al* 2020 Development and characterisation of acoustofluidic devices using detachable electrodes made from PCB *Lab Chip* **20** 1807–14
[23] Sun C, Mikhaylov R, Fu Y, Wu F, Wang H, Yuan X, Xie Z, Liang D, Wu Z and Yang X 2021 Flexible printed circuit board as novel electrodes for acoustofluidic devices *IEEE Trans. Electron Devices* **68** 393–8
[24] Barnkob R, Iranmanesh I, Wiklund M and Bruus H 2012 Measuring acoustic energy density in microchannel acoustophoresis using a simple and rapid light-intensity method *Lab Chip* **12** 2337–44
[25] Wu F *et al* 2021 An enhanced tilted-angle acoustofluidic chip for cancer cell manipulation *IEEE Electron Device Lett.* **42** 577–80
[26] Chen Y, Wu M, Ren L, Liu J, Whitley P H, Wang L and Huang T J 2016 High-throughput acoustic separation of platelets from whole blood *Lab Chip* **16** 3466–72